

## Article

# Validating Structural Styles in the Flysch Basin Northern Rif (Morocco) by Means of Thermal Modeling

Achraf Atouabat <sup>1,\*</sup>, Sveva Corrado <sup>1</sup>, Andrea Schito <sup>1</sup>, Faouziya Haissen <sup>2</sup>, Oriol Gimeno-Vives <sup>3</sup>, Geoffroy Mohn <sup>3</sup> and Dominique Frizon de Lamotte <sup>3</sup>

<sup>1</sup> Dipartimento di Scienze, Sezione di Scienze Geologiche, Università degli Studi Roma Tre, Largo San Leonardo Murialdo 1, 00146 Roma, Italy; sveva.corrado@uniroma3.it (S.C.); andrea.schito@uniroma3.it (A.S.)

<sup>2</sup> Faculté des Sciences Ben M'sik, Département de Géologie, Université Hassan II de Casablanca, Casablanca 20800, Morocco; faouziya.haissen@gmail.com

<sup>3</sup> Département Géosciences et Environnement (GEC), CY Cergy Paris Université, 95000 Cergy-Pontoise, France; oriol.gimeno@cyu.fr (O.G.-V.); geoffroy.mohn@cyu.fr (G.M.); Dominique.Frizon-de-Lamotte@cyu.fr (D.F.d.L.)

\* Correspondence: achraf.atouabat@uniroma3.it; Tel.: +39-329-932-7115

Received: 30 June 2020; Accepted: 17 August 2020; Published: 19 August 2020



**Abstract:** Vitrinite reflectance and a micro-Raman spectroscopy parameters data set have been acquired on dispersed organic matter of the Maghrebien flysch basin and the Tangiers unit across a NE-SW section in the north-western Rif belt (North Morocco). Thermal maturity shows increasing values from the hinterland to the external unit (from NE to SW). Paleo-thermal indicators show that the internal flysch basin (i.e., the Mauretanian unit) is less mature than the external one, (i.e., the Massylian unit), with  $R_o\%$  and  $R_o$  eq. Raman values ranging from 0.64% to 1.02% (from early mature to late mature stages of hydrocarbon generation). 1D thermal modeling estimates the overburden now totally eroded ranging from 3.1 km to 6.0 km, and has been used as constraint to reconstruct the complete thrust wedge geometry in Miocene times. The reconstructed geometry accounts for high shortening (about 63%) due to the development of an antiformal stack in the frontal part of the wedge made up by the flysch succession. This stacking is interpreted as a consequence of the western translation of the Alboran Domain in the core of the Betic-Rif orogenic system.

**Keywords:** Rif belt; Maghrebien Flysch basin; vitrinite reflectance; micro-Raman spectroscopy; thermal modeling; thrust wedge

## 1. Introduction

Fold-and-thrust belts are structures through which former passive margin sedimentary covers and shallow basement rocks mainly shorten because of convergence. The rules of their evolution both across and along the strike are well-known [1–5]. Nevertheless, uncertainty exists in defining the structural style and shortening in the Central-Western Mediterranean region, where orogens develop with typical arcuate shapes [6,7] as a result of the long-lasting tectonic evolution in between the convergence of Eurasia and Africa. In particular, ranges of shortening can differ up to one order of magnitude [8], with important implications on energy resource potential evaluation in structurally complex areas [9].

The Rif belt (Figure 1) is one of the most complex areas in Western Mediterranean as it is extremely arcuate [10,11]. For many decades, the area complexity has brought the development of different and sometimes contrasting geodynamic models [12]. The most accepted models that explain the evolution

of the West-Mediterranean region are: (i) convective removal of the lithospheric mantle and orogenic collapse [13], (ii) a single subduction plane with multiple roll-backs [14], (iii) the Slab retreat model [15], and more recently, (iv) the double subduction model [16].

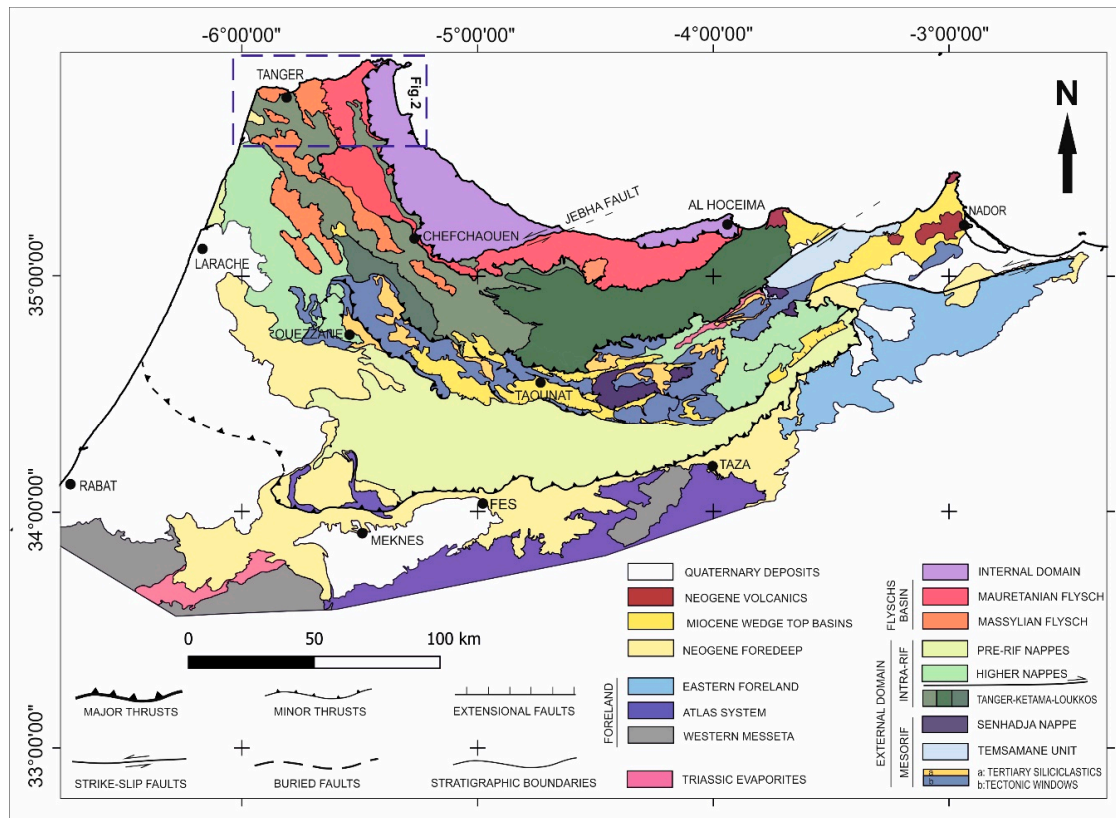


**Figure 1.** Structural sketch map of the Rif belt in northern Morocco (modified after [17–19]). Black dashed rectangle shows the location of the studied area, shown in Figure 2.

Such differences are the result of the lack or poor-quality subsurface data and/or scarce information related to the eroded portions of the belts themselves [20–23]. There is a lack of information bias on the reconstructions, mainly of the internal portions of the fold-and-thrust belts, which are characterized by intense deformation and detachments [11,24]. In such cases, structural tools, such as restoration and structural balancing techniques, allow multiple viable interpretations [25,26]. Moreover, in order to reduce the number of structural solutions, the estimation of the eroded portion of a thrust wedge through time is pivotal. To reach this aim, a useful tool is the integration of thermal modeling of sedimentary successions with section drawing [9,22,27].

In this paper, along a NE-SW regional transect crossing the Maghrebian flysch basin and the Tangiers unit (Intrarif Domain), eight 1D thermal models have been established to reconstruct the eroded portion of the shortened section to reduce uncertainties for section building. Thermal models were calibrated by the means of two different paleothermal indicators: vitrinite reflectance ( $R_o\%$ ) and  $R_o$  equivalent from Raman spectroscopy derived from analyses on dispersed organic matter.

## 2. Geological Setting

The Gibraltar arc represents the western edge of the West-Mediterranean Alpine systems. Its formation and arcuate shape [7,28,29] developed as a consequence of the westward translation of the Alboran Domain in the general framework of the Africa-Eurasia collision [30–33].

The Rif belt (Figure 1) represents the southern limb of the Gibraltar Arc. It is also a part of the Maghrebides (Tell-Rif) orogenic system [34], resulting from the progressive closure of the Maghrebian

Tethys and the final docking of the Alboran domain onto the African margin during the Late Burdigalian age [10,18,35].

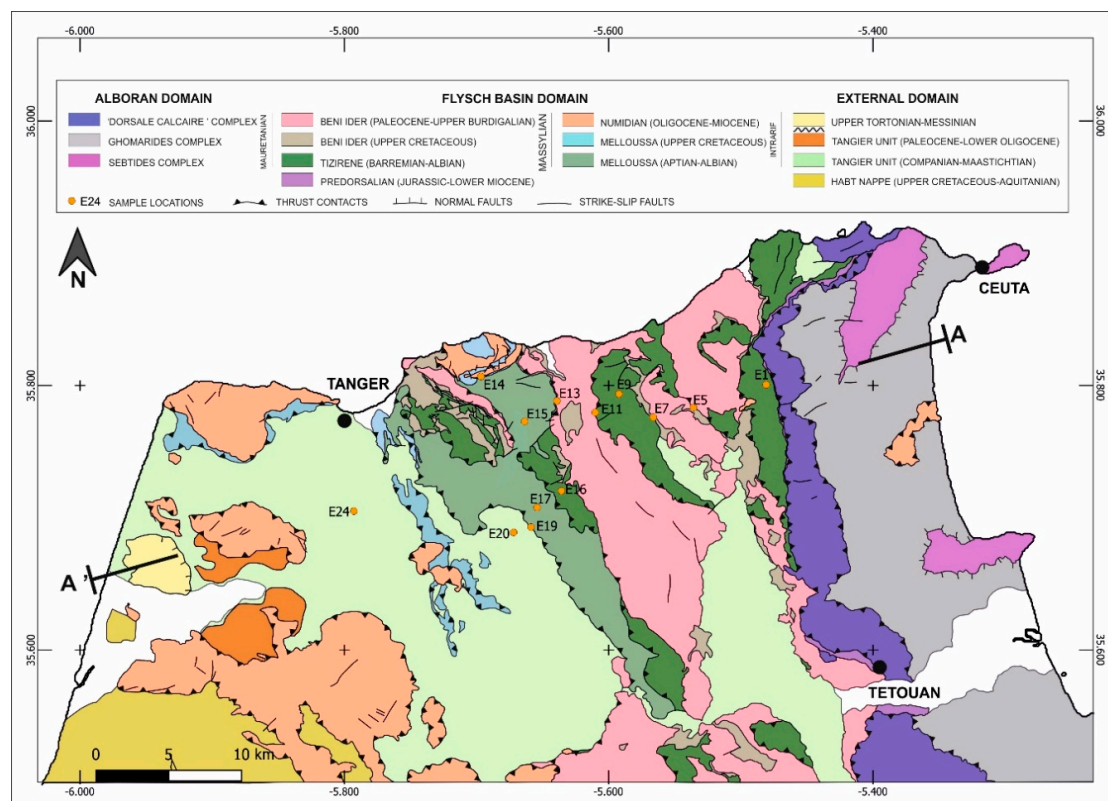


**Figure 2.** Geological map of the northwestern corner of the Rif belt with sample locations, compiled from the Geological maps of the Rif at 1/50000 published by the Geological Survey of Morocco [36–40]. A–A' refers to the studied transect (see Figure 4).

The Rif belt was built mainly during Miocene times by the interaction between the Alboran domain, the Maghrebian flysch basin, and the External domain [41,42]) toward the southwest and south (Figures 1 and 2).

The innermost Alboran domain [43,44] is derived from the northern paleo-margin of the Maghrebian Tethys and consists of the Sebides Complex [44], which corresponds to continental terranes affected by Variscan and Alpine metamorphism [45,46]; the Ghomarides complex [47,48], which is made of Paleozoic terranes affected by Variscan metamorphism [48–50], except for the lowest part, which is also affected by a localized Alpine metamorphism [51]; and the “Dorsale Calcaire,” which corresponds to Triassic-Lower Jurassic carbonates and Cenozoic siliciclastic deposits [52,53].

The Maghrebian flysch basin [10,54,55] corresponds to the Meso-Cenozoic deep marine southern branch of the Maghrebian Tethys, which was connecting the Alpine oceans with the central Atlantic from the Jurassic up to the Miocene [47,55–57]. The Maghrebian flysch basin is subdivided into internal Mauretanian and external Massylian Domains (Figure 3, [58–60]).

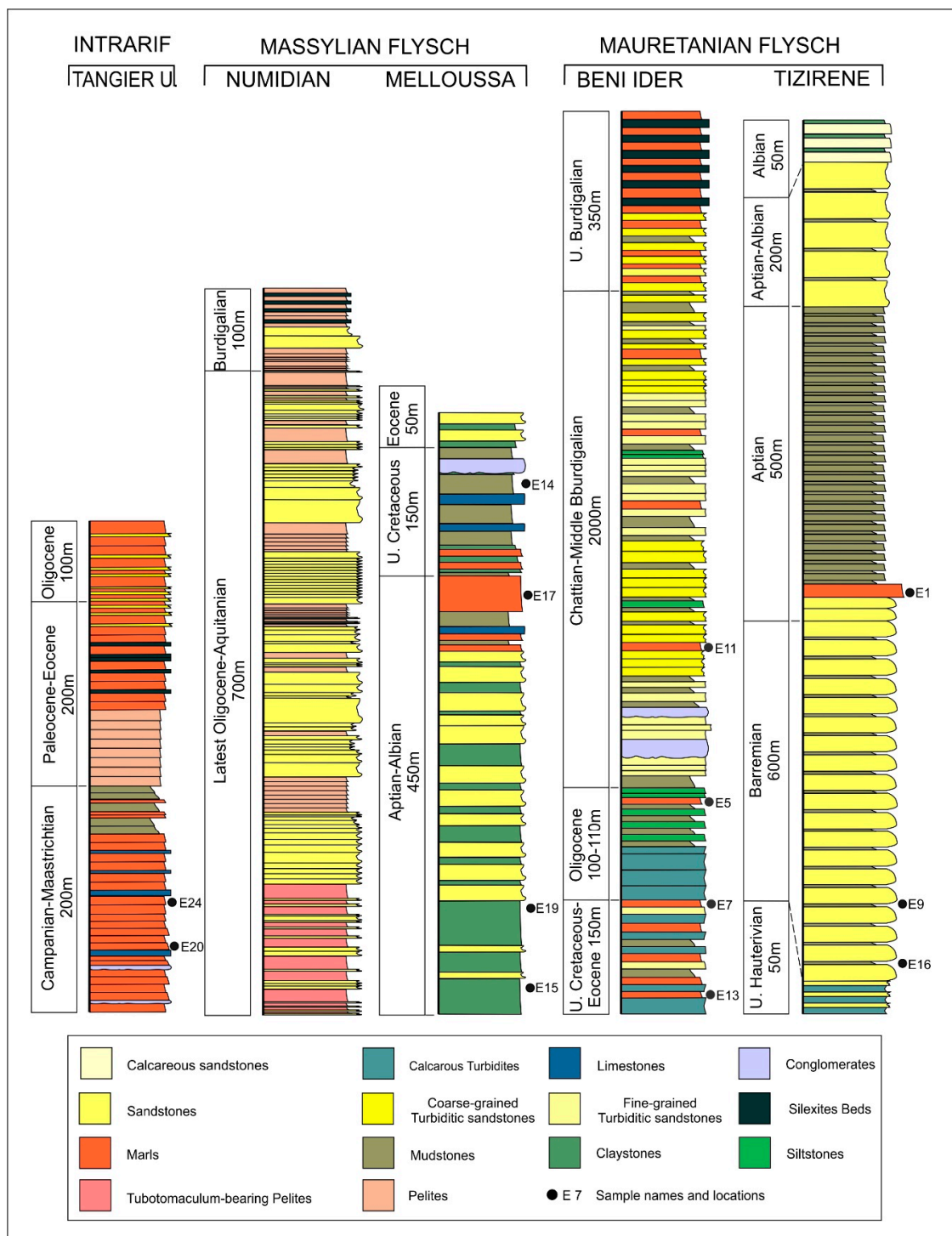


**Figure 3.** Simplified stratigraphic columns of the sampled units with sample names and positions. The stratigraphic columns are modified and/or redrawn after [18,57,61,62]. The columns are not to scale.

The transition between the two sub-domains is differentiated in the Oligocene-Lower Miocene sediments, where the Mauretanian Beni Ider turbidites evolve laterally to the Massylian Numidian sandstones through mixed successions [63–65]. During the orogenesis, the sedimentary cover of the Maghrebain flysch basin formed a series of thrust sheets (Figure 4) [65,66].



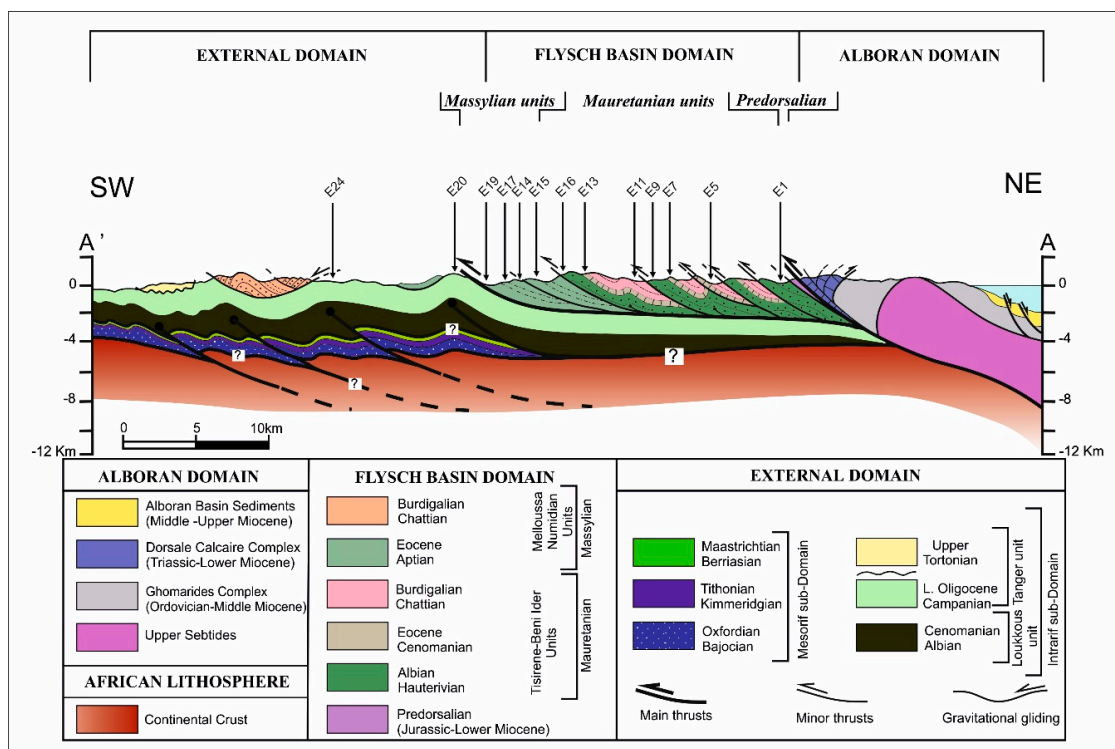


**Figure 4.** Structural cross-section (see Figure 2 for location) showing the overall architecture of the Maghrebian flysch basin and its relationship with the Internal and External domains based on [36–40] and on field observations. Sample names and position are indicated.

The external zones belongs to the North African paleomargin that was overthrust by the Internal and Flysch domains during the Cenozoic Alpine cycle [19,47,67]. The external Rif is subdivided into the Intrarif, which also organized into three main sub units, known as Ketama, Loukkos, and Tangiers units; the Mesorif; and the Prerif [17]. In front of the system, the Middle Atlas system represents the foreland of the Rif belt, where a Miocene foredeep basin developed. The latter is covered by the Prerif nappes and other more organized and far-travelled nappes (higher nappes) deriving from the Intrarif (Figure 1), namely the Aknoul, Tsoul, Habbt, and Ouezzane Nappes [10,19,68–70].

### 3. Samples and Methods

#### 3.1. Samples

Organic matter optical analysis and micro-Raman spectroscopy were performed on dispersed organic matter from thirteen samples carried out along a NE-SW transect (Figure 4). Three samples were collected from marls/mudstones levels of the Mauretanian Tizirene flysch, four samples from the marly levels of the Mauretanian Beni Ider flysch, four samples from the marl/claystone/mudstone levels of the Massylian Melloussa flysch, and two samples from the marls levels of the Intrarifain Tangier unit (Figures 2 and 3). All samples were collected far from major faults (e.g., >10 m), see (Figure 4), in order to avoid frictional heating and/or alteration effects [71].

#### 3.2. Methods

##### 3.2.1. Organic Matter Optical Analysis

Whole-rock samples were slightly crushed in an agate mortar, mounted in epoxy resin, and then polished according to standardized procedure [72]. Vitrinite reflectance ( $R_0\%$ ) measurements were performed on randomly oriented organic grains with a Zeiss Axioplan microscope, using conventional

micro-photometric methods under oil immersion ( $n = 1.518$ ) in reflected monochromatic non-polarized light ( $\lambda = 546$  nm). The calibration is based on three reflectance standards with a  $R_o\%$  values of 0.427, 0.585, and 0.905 for Spinel, Sapphire, and Yttrium-Aluminum-Garnet, respectively. The population of the measured fragment varies between eight in samples with small amounts of organic matter and 40 in organic matter-rich ones. Measurements were performed on non-oxidized fragments, never smaller than 5  $\mu\text{m}$ , only slightly fractured and/or altered [73].

### 3.2.2. Micro-Raman Spectroscopy on Organic Matter

The analysis of carbonaceous material by means of Raman spectroscopy has grown quickly in the last years. It has turned out to be a powerful geothermometer for metamorphic rocks [74–76], and recently also for coals and dispersed organic matter in diagenesis [76–86], even if a unique procedure has not still been defined [87].

In diagenesis, the first-order Raman spectra are composed by two main bands known as the D and G bands [88,89], and also other minor bands. The G band is linked to the in-plane vibration ( $E_{2g}$  symmetry) of carbon atoms in graphene in crystalline graphite at  $1582\text{ cm}^{-1}$  [88,90,91]. The D band at  $1350\text{ cm}^{-1}$  [92] becomes active in disordered graphite, and it has been interpreted as a result of a the double resonant Raman scattering process [90–92] or alternatively, it is able to rise from the ring breathing vibration in the graphite sub-units or polycyclic aromatic compounds [82,93–95] or from the aromatics with six rings or more [96]. The assignment of the other bands is still a matter of debate [85,94,96–99].

The best relationship between Raman parameters and thermal maturity in diagenesis is generally found for the full width at half maximum (FWHM) of the G and D bands, the position of the G and D band, the D/G area, and D/G intensity ratio (see [87] for a review).

Micro-Raman spectroscopic analyses were performed on whole-rock powders using a Witec-Rise Micro-Raman spectrometer, calibrated against the  $520.74\text{ cm}^{-1}$  band of silica. Data were collected over the first order Raman spectrum ( $700\text{--}2300\text{ cm}^{-1}$ ) [88], using a 600 grooves/mm grating and CCD detector. A green laser ( $\lambda = 532$  nm) with a power of 75 mW was used as light source, while the optical filters adjusted the laser power at  $<0.4$  mW. To reduce the fluorescence, the Raman backscattering was recorded after an integration time of 30 s for four repetitions [85]; then between 10 and 30 measurements per sample were performed in order to ensure reproducibility.

The first analytical process performed on the spectra was the removal of the fluorescence background interfering with the Raman spectra of highly disordered carbonaceous material [74,85]. A linear baseline subtraction has been applied at the limits of the D and G spectral regions, respectively [100]. The D band is centered at about  $1350\text{ cm}^{-1}$ , and thus, the D band region has been defined between  $1100$  and  $1470\text{ cm}^{-1}$ , while for the G centered at about  $1600\text{ cm}^{-1}$ , we defined its region between  $1450$  and  $1700\text{ cm}^{-1}$ .

Despite the fact that Raman spectroscopy has been widely used on dispersed organic matter and coals to assess thermal maturity, its application in the “oil window” is still a matter of debate, essentially due to the different curve-fitting methods in this temperature range [84,86]. In this work we adopted the automatic approach proposed by Schito and Corrado (2018) that requires a minimum data manipulation. In this method, D and G bands are fitted separately, applying a one-band asymmetrical Gaussian deconvolution for each spectral region, with an asymmetry of 65% and 60% for the D and G bands, respectively. We determined position, intensity, width, and integrated area of the D and G bands. The applicability range is between 0.3 and 1.5  $R_o\%$  [100].

The Raman spectral parameters are used to calculate the  $R_o$  equivalent % ( $R_o\%$  eq.) through a parametric equation resulting from a multi-linear regression based on a correlation between Raman parameters and vitrinite reflectance ( $R_o\%$ ) [100].

### 3.2.3. Thermal Modeling

Thermal history and burial of the northwestern side of the Maghrebien flyschs basin were performed using the Basin Mod 2-D software package by Platte River (2020). Assumptions used for the modeling are: (1) decompaction of the burial curves according to Sclater and Christie [101]; (2) thrusting duration is considered instantaneous [102]; (3) a sediment-water-interface temperature of 12 °C and a surface temperature of 20 °C are assumed; (4) burial and thermal models were constrained by organic thermal indicators (vitrinite reflectance  $R_o\%$  and  $R_o\%$  eq. [100]), and are carried out using the LLNL Easy%Ro method based on the kinetic model of vitrinite maturation of [103] and [104]; (5) heat flow is fixed at 55 mW/m<sup>2</sup> [105,106]; (6) thicknesses, lithology, and ages of sediments are from [18,57,61,62], and have been used to constrain the pseudo-wells perpendicularly to the main stratification while respecting the samples positions; (7) finally, the sea-level variations are neglected, as the thermal evolution is mainly controlled by sediments thickness [107].

## 4. Results

### 4.1. Organic Matter Optical Analysis

Vitrinite reflectance values in the area vary between 0.64 and 1.02% (Table 1).

**Table 1.** Organic matter maturity derived from vitrinite reflectance ( $R_o\%$ ) and micro-Raman spectroscopy ( $R_o\%$  eq.) analyses.

| UNIT        | SAMPLES | COORDINATES                  | AGES             | $R_o\%$ | Sd. (±) | Nr. Fr | $R_o\%$ eq. | Sd. (±) |
|-------------|---------|------------------------------|------------------|---------|---------|--------|-------------|---------|
| MAURETANIAN | E1      | 35.80055556;<br>−5.480833333 | Aptian           | 0.64    | 0.08    | 9      | —           | —       |
|             | E5      | 35.78333333;<br>−5.535833333 | Oligocene        | 0.92    | 0.08    | 16     | —           | —       |
|             | E7      | 35.775963;<br>−5.566249111   | Eocene           | 0.65    | 0.08    | 12     | —           | —       |
|             | E9      | 35.79361111;<br>−5.592222222 | Barremian        | 0.75    | 0.07    | 23     | —           | —       |
|             | E11     | 35.77958303;<br>−5.610247222 | Miocene          | 1.00    | 0.08    | 40     | —           | —       |
|             | E13     | 35.78833333;<br>−5.639166667 | Campanian        | 0.84    | 0.04    | 8      | 0.86        | 0.08    |
|             | E16     | 35.72027778;<br>−5.635833333 | Barremian        | 0.98    | 0.05    | 29     | —           | —       |
| MASSYLIAN   | E15     | 35.77277778;<br>−5.663611111 | Aptian           | 1.01    | 0.07    | 18     | 1.00        | 0.08    |
|             | E14     | 35.80676;<br>−5.696666       | U.<br>Cretaceous | 0.77    | 0.06    | 20     | —           | —       |
|             | E17     | 35.70777778;<br>−5.654166667 | Albian           | 1.00    | 0.05    | 28     | 0.98        | 0.07    |
|             | E19     | 35.69285255;<br>−5.658765111 | Aptian           | 0.82    | 0.06    | 33     | 0.90        | 0.10    |
| INTRARIF    | E20     | 35.68888889;<br>−5.671944444 | Campanian        | 1.02    | 0.06    | 30     | 1.06        | 0.06    |
|             | E24     | 35.705;<br>−5.792777778      | Campanian        | 0.87    | 0.09    | 24     | 0.88        | 0.10    |

Coordinates system: “WGS-84”; Sd. (±): standard deviation; Nr. Fr: number of fragments.

The Mauretanian Tizirene unit constitutes four thrust sheets (Figure 4). The three samples studied along the NE-SW transect (Figures 2 and 4) contain well-preserved fragments belonging to both the vitrinite and inertinite maceral groups. The  $R_o\%$  values increase from internal to external thrust sheets according to their depth and structural position, and range from 0.64% to 0.98% (Figures 3–5), indicating the early to middle stages of oil generation [108].

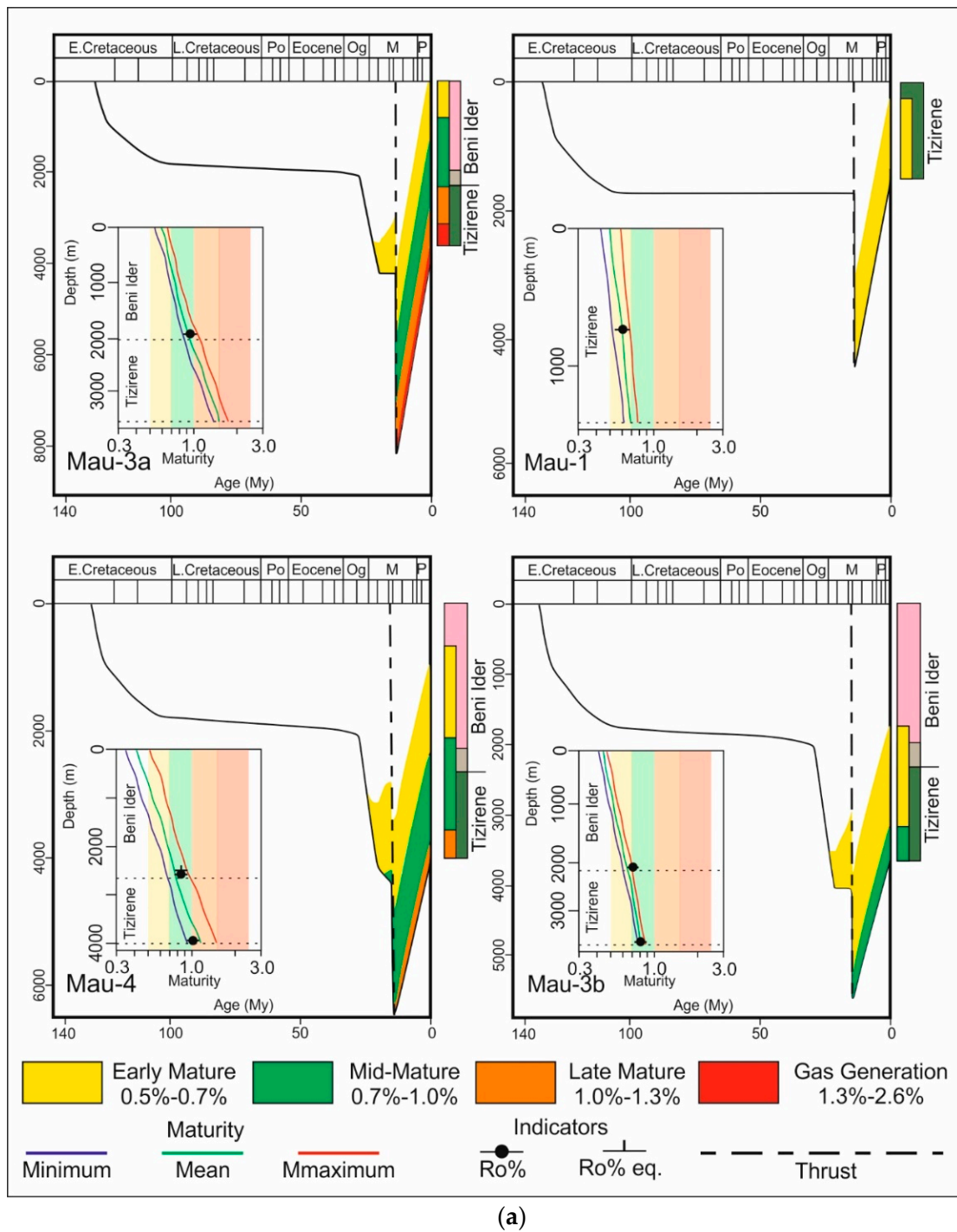
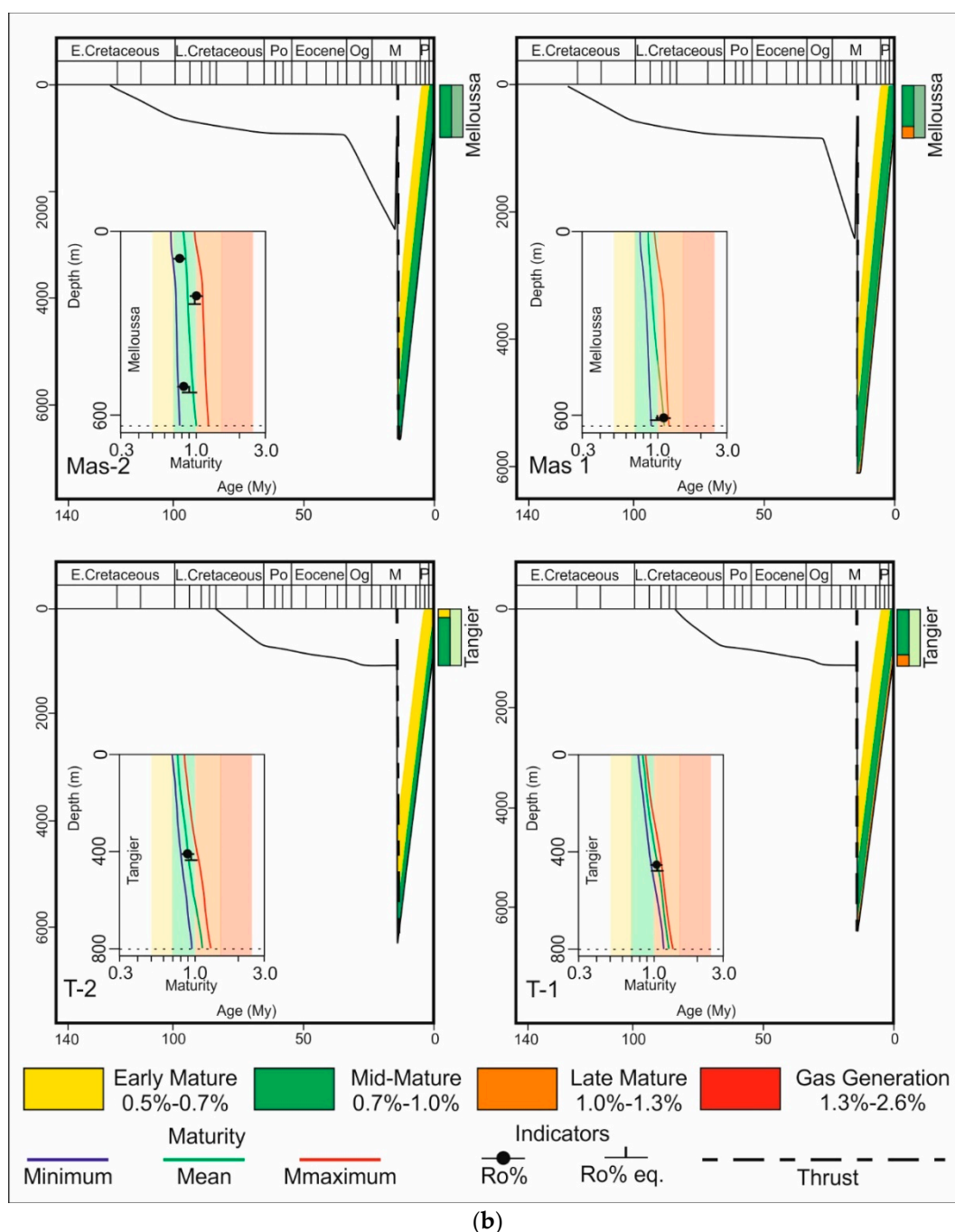


Figure 5. Cont.





**Figure 5.** (a) Burial and thermal models of the Mauretanian thrust sheets showing maturity versus depth and hydrocarbon generations. Diagrams constrained by vitrinite reflectance  $R_o\%$  and  $R_o\%$  equivalent (calculated from Raman parameters). For detailed lithology, see Figure 3. Mau-(1, 3.a., 3. b., and 4): pseudo-wells belonging to each thrust sheet. Po—Paleocene, Og—Oligocene, M—Miocene, and P—Pliocene; (b). Burial and thermal models of the Massylian thrust sheets and Tangier unit showing maturity versus depth and hydrocarbon generations. Diagrams constrained by vitrinite reflectance  $R_o\%$  and  $R_o\%$  equivalent (calculated from Raman parameters). For detailed lithology, see Figure 3. Mas-1 and Mas-2: pseudo-wells belonging to the Massylian thrust sheets; T-1 and T-2: pseudo-wells belonging to Tangier unit. Po—Paleocene, Og—Oligocene, M—Miocene, and P—Pliocene.

The Mauretanian Beni Ider unit is comprised of three thrust sheets (Figure 4) and contain well-preserved vitrinite and inertinite. The  $R_o\%$  values vary between 0.65% and 1.00 % (Table 1), increasing from internal to external thrust sheets outlining maturities in the middle mature stages of

hydrocarbon generation. Vitrinite reflectance data from the Beni Ider unit show two different levels of thermal maturity along the transect, depending on the samples position with respect to the upper thrust.  $R_o\%$  values range from 0.65% to 0.84% when they are far from the tectonic contacts, and from 0.92% to 1.00% when the samples lie just below the upper thrust.

The Massylian flysch domain is represented by the Melloussa unit, composed of two thrust sheets (Figure 4). The four collected samples show the presence of both vitrinite and inertinite macerals groups.  $R_o\%$  values range between 0.77% and 1.01%, indicating the middle mature stage of hydrocarbon generation. The obtained values show a trend of increasing maturity with stratigraphic depth. Locally, shallow samples located at the footwall of the thrust separating the two thrust sheets show slightly higher values (Figures 3 and 4). Generally, the average values of  $R_o\%$  in the Melloussa unit are higher than in the Tizirene and Beni Ider units.

The Tangiers unit (Figures 2–4, and Table 1) provides  $R_o\%$  values of 1.02% at the footwall of the regional thrust located between the Maghrebian flysch basin domain and the Intrarif domain, and the 0.87% moving externally toward the West. The obtained values indicate the middle mature stage of hydrocarbon generation.

#### 4.2. Micro-Raman Spectroscopy on Organic Matter

From the thirteen collected samples, six were suitable for micro-Raman spectroscopic analysis. However, all along the NE-SW section presented in Figure 4, the  $R_o\%$  equivalent values derived from the Raman spectra are highly consistent with the measured vitrinite reflectance  $R_o\%$  (Table 1). In the Mauretanian Beni Ider unit, the  $R_o\%$  equivalent value calculated from the Raman spectra is 0.86%. In the Massylian Melloussa unit, the  $R_o\%$  equivalent values are between 0.90 and 1.00%. In the Tangiers unit, the  $R_o\%$  equivalent values are 1.06% and 0.88%.

### 5. Discussion

Vitrinite reflectance is the most widespread thermal maturity indicator in the diagenetic realm [109], while Raman spectroscopy on organic matter has been widely debated, especially when related to thermal maturity assessment in diagenesis [77,85,87,110,111].

The use of different thermal maturity indicators in the thermal model is highly recommended since it has been demonstrated that vitrinite reflectance alone can suffer several pitfalls due to the scarcity or misidentification of maceral content, or reflectance retardation/suppression phenomena [112]. Due to scarcity or uncertainties derived from a small dimension of vitrinite fragments, we decided to couple optical analyses with Raman analyses on organic matter using the equation proposed by [100]. The good agreement between the two methods makes our results particularly reliable for thermal model calibration. Moreover, in order to provide a large spectrum of solutions, three different burial-thermal scenarios are presented providing minimum, mean, and maximum values. Among them, the mean values are used to discuss the overburden calculation for sake of simplicity. Two wells (Mau-3a and Mau-1) were calibrated with only one set of thermal maturity data, which is not usually considered enough to ensure model reliability. Nevertheless, assuming no significant variation in the heat flow regime, one point on the calibration curve can be sufficient to evaluate the magnitude of the tectonic burial.

In the Maghrebian flysch basin (Figures 1 and 2), the evolution of the Mauretanian succession started in Lower-Cretaceous times with the deposition of the Tizirene turbiditic flysch (Figure 3), and continues up to the Late-Burdigalian with the deposition of the Beni Ider siliciclastic sediments, which become gradually thicker toward the external portion of the Mauretanian basin [57]. During the Alpine orogeny, between the Late Burdigalian and Early Langhian, the Mauretanian and Massylian flysch were involved in the advancing of the orogenic wedge [66,113]. The compressive event affecting the Maghrebian flysch was expressed by four NE-SW thrusts sheets. Thermal models performed for the Mauretanian flysch basin show an increase of overburden moving from the most internal thrust

sheet to the most external one (Figure 5a), varying from 3.1 km in the more internal thrust (Mau-1), located immediately at the footwall of the ‘Dorsale Calcaire’, to 4.2 km in Mau-4 (Figures 4 and 6).

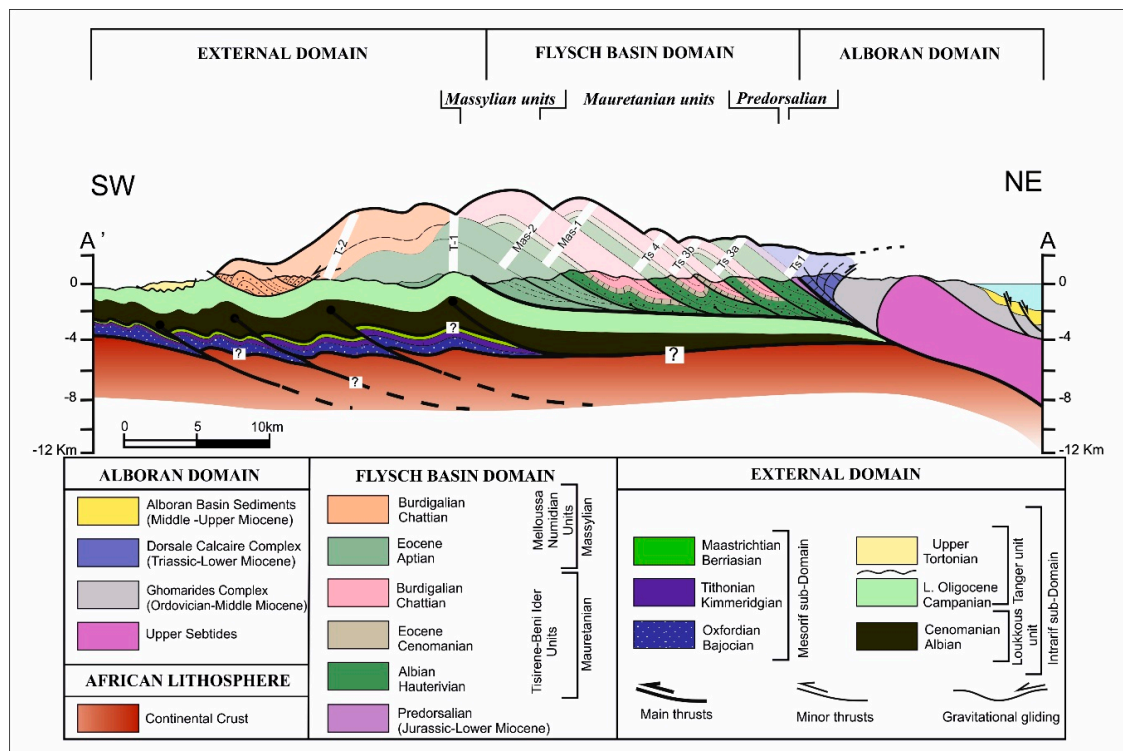


**Figure 6.** Structural cross sections showing the envelope of the paleo-wedge in Miocene times (black dashed bold line) and calculated tectonic loads. White bars represent the locations where thermal models were performed.

Moving toward the SW, the Massylian flysch basin was deformed into two thrust sheets (Mas-1 and Mas-2) (Figures 4 and 6) with a NE-SW direction. Two thermal models have been performed in the Massylian domain (Figure 5b). The evolution started from the Aptian-Albian times with the deposition of the Melloussa flysch, up to Late-Burdigalian marking the end of the thick Numidian sandstones deposition. In Langhian times, the Massylian successions suffered a tectonic burial of 5.4 km on Mas-1 and 6 km on Mas-2 (Figure 6). The emplacement of this tectonic load is synchronous with the activation of a regional flat within the Massylian domain between Melloussa and the Numidian. This detachment allowed the Numidian sandstone to glide in front of the Massylian domain onto the Tangiers unit. Accordingly, this succession experienced deep diagenetic conditions and a middle-mature stage of hydrocarbon generation.

More externally, two thermal models have been performed for the Tangiers unit, whose sedimentation started in Late Cretaceous time. During the progressive advancing of the wedge, the Tangiers unit underwent a tectonic burial at about -14 Ma ranging between 5.5 km (T-1) and 5 km (T-2) Figure 5b and Figure 6).

The discrimination between the sedimentary and tectonic contribution to the burial paths in the flysch basin is well constrained. First of all, the stratigraphy was defined by previous literature (Figure 3). Furthermore, possible younger sediments (unconformable Pliocene deposits [57]) crop up to the south of the study area, but are not recognized along the studied transect. Such evidence suggests that the overburden calculated from the models along the studied transect could be due to thrusting. These considerations allowed us to define the envelope of the thrust wedge by the projection of the calculated loads derived from thermal modeling onto the cross section (Figure 4), and to reconstruct the shape of the accretionary wedge in Miocene times before erosion (Figure 6).

The reconstructed wedge becomes higher toward its external part, shedding light on the lack of cylindricity along-strike in the fold and thrust belts, which is commonly expressed by the variation of structural styles and shortening rates [5]. Strike-slip faults are considered one of the main factors controlling the along-strike variations (e.g., [114]), and are usually debated in kinematic reconstructions. This feature should not be neglected in the Rif belt that is affected by the Jebha regional left-lateral strike-slip fault. The latter caused considerable differences in the geometry and internal deformation organization on both sides of the fault [115–118], and by consequence, controlled the shortening rates in the terranes cropping up north and south of this lineament (Figure 1). We suggest that the propagation of the orogenic wedge may be enhanced by this along-strike variation leading to the development of a thrust sheet stacking, which can be explained by the acquired tectonic loading and the 62.8% rate of shortening (Figure 6). Additionally, it is assumed that the Maghrebien flysch basin was deposited on an oceanic or thinned continental crust [10,54,56,57,65,113] bordered southward by the north African paleomargin, nowadays represented by the Intrarif. The latter may act as a bulge controlling the frontal propagation of the wedge, due to crustal thickness contrast. We consider this feature responsible for the development of the antiformal stacking in the most external side of the Maghrebien flysch basin, which is expressed by a tectonic loading reaching 6.0 km of thickness (Figure 6). In conclusion, we suggest that the shape of the reconstructed wedge during Miocene times (Figure 6) is, on one hand, the result of compressive tectonic events due to the Africa-Iberia convergence and the Alboran domain translation during the Alpine orogeny. This process is probably enhanced by the role of the Jebha fault and the north African paleomargin that acted as a bulge blocking the wedge propagation.

## 6. Conclusions

Organic thermal maturity within the flysch basin of the Rif belt shows a general increase moving from internal to external portions of the fold-and-thrust belt. Levels of thermal maturity for the outcropping successions range from early-mature to late-mature stages of hydrocarbon generation. Combining thermal modeling and the present-day geometry of the wedge, we can reconstruct the shape of the thrust wedge in Miocene times, which shows an increase in thickness moving toward the southwest (i.e., North African paleomargin) with tectonic loads ranging from 3.1 km to 6.0 km. The high shortening of 63% within the Maghrebien flysch basin highlighted the role played by the Jebha fault in the thrust wedge evolution as suggested by previous authors [115–118]. Both the thrust wedge propagation and the pre-orogenic geometry of the Maghrebien flysch basin and related margins are responsible for the formation of numerous thrust sheets and the development of an antiformal stacking at the front of the wedge, shortening the flysch basin domain.

**Author Contributions:** Conceptualization, A.A., S.C., A.S., G.M. and D.F.d.L.; methodology, A.A., S.C. and A.S.; software, A.A., A.S. and S.C.; investigation, A.A., S.C., F.H. and O.G.-V.; resources, S.C. and G.M.; data curation, A.A.; writing—original draft preparation, A.A.; writing—review and editing, A.A., S.C., A.S., F.H., O.G.-V., G.M. and D.F.d.L.; visualization, A.A.; supervision, S.C., A.S. and G.M.; project administration, S.C.; funding acquisition, S.C., G.M. and D.F.d.L. All authors have read and agreed to the published version of the manuscript.

**Funding:** This research was funded by: The Grant of Excellence Departments, MIUR-Italy (ARTICOLO 1, COMMI 314–337 LEGGE 232/2016) and the financial support of the PhD School in Earth Sciences of Roma Tre University.

**Acknowledgments:** Organic petrography has been performed in ALBA (Academic Laboratory of Basin Analysis) of Department of Science of “Roma Tre” University. The authors are grateful to Philippe Robion, responsible of the “Integrated microscopic Platform” in CY Cergy Paris Université where micro-Raman spectroscopy on dispersed organic matter has been performed. M. N. Zaghloul from “Abdelmalek Essaâdi” University is warmly acknowledged for exciting discussions on Rif geology and geodynamic evolution and great days in the field in the early phase of the research.

**Conflicts of Interest:** The authors declare no conflict of interest.

## References

1. Dahlstrom, C.D.A. Balanced cross sections. *Can. J. Earth Sci.* **1969**, *6*, 743–757. [[CrossRef](#)]
2. Boyer, S.E.; Elliott, D. Thrust systems. *Am. Assoc. Pet. Geol. Bull.* **1982**. [[CrossRef](#)]

3. Butler, R.W.H. Thrust sequences. *J. Geol. Soc. Lond.* **1987**, *144*, 619–634. [\[CrossRef\]](#)
4. Willett, S.D.; Beaumont, C.; Fullsack, P. Mechanical Model for doubly vergent compressional orogens. *Geology* **1993**, *21*, 371–374. [\[CrossRef\]](#)
5. Butler, R.W.H.; Mazzoli, S. Styles of continental contraction: A review and introduction. *Spec. Pap. Geol. Soc. Am.* **2006**, *414*. [\[CrossRef\]](#)
6. Cifelli, F.; Mattei, M.; Porreca, M. New paleomagnetic data from Oligocene-upper Miocene sediments in the Rif chain (northern Morocco): Insights on the Neogene tectonic evolution of the Gibraltar arc. *J. Geophys. Res. Solid Earth* **2008**, *113*, 1–12. [\[CrossRef\]](#)
7. Royden, L.; Faccenna, C. Subduction Orogeny and the Late Cenozoic Evolution of the Mediterranean Arcs. *Annu. Rev. Earth Planet. Sci.* **2018**, *46*, 261–289. [\[CrossRef\]](#)
8. Tozer, R.S.J.; Butler, R.W.H.; Corrado, S. Comparing thin- and thick-skinned thrust tectonic models of the Central Apennines, Italy. *Stephan Mueller Spec. Publ. Ser.* **2001**, *1*, 181–194. [\[CrossRef\]](#)
9. Balestra, M.; Corrado, S.; Aldega, L.; Rudkiewicz, J.L.; Gasparo Morticelli, M.; Sulli, A.; Sassi, W. 3D structural modeling and restoration of the Apennine-Maghrebian chain in Sicily: Application for non-cylindrical fold-and-thrust belts. *Tectonophysics* **2019**, *761*, 86–107. [\[CrossRef\]](#)
10. Leprêtre, R.; de Lamotte, D.F.; Combier, V.; Gimeno-Vives, O.; Mohn, G.; Eschard, R. The Tell-Rif orogenic system (Morocco, Algeria, Tunisia) and the structural heritage of the southern Tethys margin. *BSGF Earth Sci. Bull.* **2018**, *189*, 10. [\[CrossRef\]](#)
11. Gimeno-Vives, O.; de Lamotte, D.F.; Leprêtre, R.; Haissen, F.; Atouabat, A.; Mohn, G. The structure of the Central-Eastern External Rif (Morocco); Poly-phased deformation and role of the under-thrusting of the North-West African paleo-margin. *Earth Sci. Rev.* **2020**, *205*, 103198. [\[CrossRef\]](#)
12. Casciello, E.; Fernández, M.; Vergés, J.; Cesarano, M.; Torne, M. The Alboran domain in the western Mediterranean evolution: The birth of a concept. *Bull. Soc. Geol. Fr.* **2015**, *186*, 371–384. [\[CrossRef\]](#)
13. Platt, J.P.; Vissers, R.L.M. Extensional collapse of thickened continental lithosphere: A working hypothesis for the Alboran Sea and Gibraltar arc. *Geology* **1989**, *17*, 540–543. [\[CrossRef\]](#)
14. Lonergan, L.; White, N. Origin of the Betic-Rif mountain belt. *Tectonics* **1997**, *16*, 504–522. [\[CrossRef\]](#)
15. Spakman, W.; Wortel, R. A tomographic view on western Mediterranean geodynamics. In *The TRANSMED Atlas. The Mediterranean Region from Crust to Mantle*; Cavazza, W., Roure, F., Spakman, W., Stampfli, G.M., Ziegler, P.A., Eds.; Springer: Berlin/Heidelberg, Germany, 2004; pp. 31–52.
16. Vergés, J.; Fernández, M. Tethys-Atlantic interaction along the Iberia-Africa plate boundary: The Betic-Rif orogenic system. *Tectonophysics* **2012**, *579*, 144–172. [\[CrossRef\]](#)
17. Suter, G. *Carte Géologique de la Chaîne Rifaine 1:500,000*; Service géologique du Maroc, BRGM: Orléans, France, 1980.
18. Chalouan, A.; Michard, A.; El Kadiri, K.; Negro, F.; de Lamotte, D.F.; Soto, J.-I.; Saddiqi, O. The Rif belt. In *The Geology of Morocco*; Michard, A., Ed.; Springer: Berlin, Germany, 2008. [\[CrossRef\]](#)
19. Gimeno-Vives, O.; Mohn, G.; Bosse, V.; Haissen, F.; Zaghloul, M.N.; Atouabat, A.; de Lamotte, D.F. The Mesozoic Margin of the Maghrebian Tethys in the Rif Belt (Morocco): Evidence for Polyphase Rifting and Related Magmatic Activity. *Tectonics* **2019**, *38*, 2894–2918. [\[CrossRef\]](#)
20. Di Paolo, L.; Aldega, L.; Corrado, S.; Mastalerz, M. Maximum burial and unroofing of Mt. Judica recess area in Sicily: Implication for the Apenninic-Maghrebian wedge dynamics. *Tectonophysics* **2012**, *530–531*, 193–207. [\[CrossRef\]](#)
21. Carlini, M.; Artoni, A.; Aldega, L.; Balestrieri, M.L.; Corrado, S.; Vescovi, P.; Bernini, M.; Torelli, L. Exhumation and reshaping of far-travelled/allochthonous tectonic units in mountain belts. New insights for the relationships between shortening and coeval extension in the western Northern Apennines (Italy). *Tectonophysics* **2013**, *608*, 267–287. [\[CrossRef\]](#)
22. Caricchi, C.; Aldega, L.; Corrado, S. Reconstruction of maximum burial along the Northern Apennines thrust wedge (Italy) by indicators of thermal exposure and modeling. *GSA Bull.* **2015**, *127*, 428–442. [\[CrossRef\]](#)
23. Balestra, M.; Corrado, S.; Aldega, L.; Morticelli, M.G.; Sulli, A.; Rudkiewicz, J.; Sassi, W. Thermal and structural modeling of the Scillato wedge-top basin source- to-sink system: Insights into Sicilian fold-and-thrust belt building (Italy). *Geol. Soc. Am.* **2019**, 1–20. [\[CrossRef\]](#)
24. Corrado, S.; Aldega, L.; Balestrieri, M.L.; Maniscalco, R.; Grasso, M. Structural evolution of the sedimentary accretionary wedge of the alpine system in Eastern Sicily: Thermal and thermochronological constraints. *Bull. Geol. Soc. Am.* **2009**, *121*, 1475–1490. [\[CrossRef\]](#)



25. Bond, C.E.; Gibbs, A.D.; Shipton, Z.K.; Jones, S. What do you think this is? “Conceptual uncertainty” in geoscience interpretation. *GSA Today* **2007**, *17*, 4–10. [[CrossRef](#)]
26. Bond, C.E.; Johnson, G.; Ellis, J.F. Structural model creation: The impact of data type and creative space on geological reasoning and interpretation. *Geol. Soc. Spec. Publ.* **2015**, *421*, 83–97. [[CrossRef](#)]
27. Hardebol, N.J.; Callot, J.P.; Bertotti, G.; Faure, J.L. Burial and temperature evolution in thrust belt systems: Sedimentary and thrust sheet loading in the SE Canadian Cordillera. *Tectonics* **2009**, *28*, 1–28. [[CrossRef](#)]
28. Rosenbaum, G.; Lister, G.S. Formation of arcuate orogenic belts in the western Mediterranean region. *Spec. Pap. Geol. Soc. Am.* **2004**, *383*, 41–56. [[CrossRef](#)]
29. Crespo-Blanc, A.; Comas, M.; Balanyá, J.C. Clues for a Tortonian reconstruction of the Gibraltar Arc: Structural pattern, deformation diachronism and block rotations. *Tectonophysics* **2016**, *683*, 308–324. [[CrossRef](#)]
30. Docherty, C.; Banda, E. Evidence for the eastward migration of the Alboran Sea based on regional subsidence analysis: A case for basin formation by delamination of the subcrustal lithosphere? *Tectonics* **1995**, *14*, 804–818. [[CrossRef](#)]
31. Pérouse, E.; Vernant, P.; Chéry, J.; Reilinger, R.; McClusky, S. Active surface deformation and sub-lithospheric processes in the western Mediterranean constrained by numerical models. *Geology* **2010**, *38*, 823–826. [[CrossRef](#)]
32. Platt, J.P.; Behr, W.M.; Johanesen, K.; Williams, J.R. The Betic-Rif Arc and Its Orogenic Hinterland: A Review. *Annu. Rev. Earth Planet Sci.* **2013**, *41*, 313–357. [[CrossRef](#)]
33. Van Hinsbergen, D.J.J.; Vissers, R.L.M.; Spakman, W. Origin and consequences of western Mediterranean subduction, rollback, and slab segmentation. *Tectonics* **2014**, *33*, 393–419. [[CrossRef](#)]
34. Durand-Delga, M.; Fontboté, J.M. Le cadre structurale de la Méditerranée occidentale. In *Les Chaînes Alpines Issues de la Téthys, Proceedings of the 26e Congrès Géologique International, Paris, France, 7–17 July 1980*; Broché: Paris, France, 1980.
35. Chalouan, A.; Michard, A. The Alpine Rif belt (Morocco): A case of mountain building in a subduction-subduction-transform fault triple junction. *Pure Appl. Geophys.* **2004**, *161*, 489–519. [[CrossRef](#)]
36. Kornprobst, J.; Durand-Delga, M. Carte Géologique du Rif, Sebta, Maroc. 1: 50000. In *Notes et Mémoires N 291*; Service géologique du Maroc: Rabat, Maroc, 1985.
37. Kornprobst, J.; Durand-Delga, M.; Faure-Muret, A.; Griffon, J.C.; Uttinger, J.; Leikine, M.; Raoult, J.F. Carte géologique du Rif, Tetouan-Ras Mazari, Maroc. 1: 50000. In *Notes et Mémoires N 292*; Service géologique du Maroc: Rabat, Maroc, 1985.
38. Durand-Delga, M.; Didon, J. Carte géologique du Rif, Ksar Es Srhir, Maroc. 1: 50000. In *Notes et Mémoires N 295*; Service géologique du Maroc: Rabat, Maroc, 1984.
39. Durand-Delga, M. Carte géologique du Rif, Melloussa, Maroc. 1: 50000. In *Notes et Mémoires N 296*; Service géologique du Maroc: Rabat, Maroc, 1984.
40. Durand-Delga, M.; Didon, J.; Médioni, R.; Wernli, R.; Suter, G. Carte géologique du Rif, Tanger-Al Manzla, Maroc. 1: 50000. In *Notes et Mémoires N 294*; Service géologique du Maroc: Rabat, Maroc, 1985.
41. Favre, P.; Stampfli, G.M. From rifting to passive margin: The examples of the Red Sea, Central Atlantic and Alpine Tethys. *Tectonophysics* **1992**, *215*, 69–97. [[CrossRef](#)]
42. de Lamotte, D.F.; Raulin, C.; Mouchot, N.; Wrobel-Daveau, J.-C.; Blanpied, C.; Ringenbach, J.-C. The southernmost margin of the Tethys realm during the Mesozoic and Cenozoic: Initial geometry and timing of the inversion processes. *Tectonics* **2011**, *30*. [[CrossRef](#)]
43. Bouillin, J. Le “bassin maghrebin”; une ancienne limite entre l’Europe et l’Afrique à l’ouest des Alpes. *Bull. Soc. Géol. Fr.* **1986**, *2*, 547–558. [[CrossRef](#)]
44. Milliard, Y. Les massifs métamorphiques et ultrabasiques de la zone paléo-zoïque interne du Rif. *Notes Mem. Serv. Géol. Maroc* **1959**, *18*, 125–160.
45. Kornprobst, J. Signification structurale des peridotites dans l’orogène betico-rifain; arguments tirés de l’étude des détritiques observés dans les sédiments paléozoïques. *Bull. Soc. Géol. Fr.* **1976**, *7*, 607–618. [[CrossRef](#)]
46. Rossetti, F.; Theye, T.; Lucci, F.; Bouybaouene, M.L.; Dini, A.; Gerdes, A.; Phillips, D.; Cozzupoli, D. Timing and modes of granite magmatism in the core of the Alboran Domain, Rif chain, northern Morocco: Implications for the Alpine evolution of the western Mediterranean. *Tectonics* **2010**, *29*. [[CrossRef](#)]
47. Wildi, W. La chaîne tello-rifaine (Algérie, Maroc, Tunisie): Structure, stratigraphie et évolution du Trias au Miocène. *Rev. Geogr. Phys. Geol. Dyn.* **1983**, *24*, 201–297.

48. Chalouan, A. Les Nappes Ghomarides (Rif Septentrional, Maroc). Un Terrain Varisque dans la Chaîne Alpine. Ph.D. Thesis, Université Louis Pasteur de Strasbourg, Strasbourg, France, 1986.
49. Chalouan, A.; Michard, A. The Ghomarides nappes, Rif coastal range, Morocco: A variscan chip in the Alpine belt. *Tectonics* **1990**, *9*, 1565–1583. [\[CrossRef\]](#)
50. Zaghloul, M.N.; Di Staso, A.; Hlila, R.; Perrone, V.; Perrotta, S. The oued dayr formation: First evidence of a new miocene late-orogenic cycle on the ghomaride complex (Internal domains of the rifian maghrebien chain, Morocco). *Geodin. Acta* **2010**, *23*, 185–194. [\[CrossRef\]](#)
51. Negro, F.; Beyssac, O.; Goffé, B.; Saddiqi, O.; Bouybaouène, M.L. Thermal structure of the Alboran Domain in the Rif (northern Morocco) and the Western Betics (southern Spain). Constraints from Raman spectroscopy of carbonaceous material. *J. Metamorph. Geol.* **2006**, *24*, 309–327. [\[CrossRef\]](#)
52. Wildi, W.; Nold, M.; Uttinger, J. La Dorsale calcaire entre Tetouan et Assifane (Rif interne, Maroc). *Ecol. Geol. Helv.* **1977**, *70*, 371–415.
53. El Kadiri, K.; Linares, A.; Oloriz, F. La Dorsale calcaire rifaine (Maroc septentrional): Evolution stratigraphique et géodynamique durant le Jurassique-Crétacé. *Notes Mém. Serv. Géol.* **1992**, *366*, 217–265.
54. Guerrero, F.; Martín-Martín, M.; Perrone, V.; Tramontana, M. Tectono-sedimentary evolution of the southern branch of the Western Tethys (Maghrebien Flysch Basin and Lucanian Ocean): Consequences for Western Mediterranean geodynamics. *Terra Nov.* **2005**, *17*, 358–367. [\[CrossRef\]](#)
55. De Capoa, P.; D’errico, M.; Di Staso, A.; Perrone, V.; Zaghloul, M.N. *Biostratigraphic constraints for the paleogeographic and tectonic evolution of the Alpine central-western Mediterranean chains (Betic, Maghrebien and Apenninic chains)*; CINECA IRIS: Bari, Italy, 2013.
56. Durand-Delga, M.; Rossi, P.; Olivier, P.; Puglisi, D. Situation structurale et nature ophiolitique de roches basiques jurassiques associées aux flyschs maghrebins du Rif (Maroc) et de Sicile (Italie). *C. R. Acad. Sci.* **2000**, *331*, 29–38. [\[CrossRef\]](#)
57. Zaghloul, M.N.; Di Staso, A.; De Capoa, P.; Perrone, V. Occurrence of upper Burdigalian silexite beds within the Beni Ider Flysch Fm. in the Ksar-es-Seghir area (Maghrebien Flysch Basin, Northern Rif, Morocco): Stratigraphic correlations and geodynamic implications. *Boll. Soc. Geol. Ital.* **2007**, *126*, 223–239.
58. Azdimousa, A.; Jabaloy-sánchez, A.; Talavera, C.; Asebriy, L.; González-lodeiro, F.; Evans, N.J. Detrital zircon U-Pb ages in the Rif Belt (northern Morocco): Paleogeographic implications. *Gondwana Res.* **2019**, *70*, 133–150. [\[CrossRef\]](#)
59. Bouillin, J.P.; Durand-Delga, M.; Gelard, J.P.; Leikine, M.; Raoult, J.F.; Raymond, D.; Tefiani, M.; Vila, J.M. Définition d’un flysch massylien et d’un flysch maurétanien au sein des flyschs allochtones de l’Algérie. *C. R. Acad. Sci. Paris* **1970**, *270*, 2249–2252.
60. Dercourt, J.; Zonenshain, L.P.; Ricou, L.E.; Kazmin, V.G.; Le Pichon, X.; Knipper, A.L.; Grandjacquet, C.; Sbertshikov, I.M.; Geyssant, J.; Lepvrier, C.; et al. Geological evolution of the tethys belt from the atlantic to the pamirs since the LIAS. *Tectonophysics* **1986**, *123*, 241–315. [\[CrossRef\]](#)
61. Durand-Delga, M.; Gardin, S.; Olivier, P. Datation des flyschs eocretacés mauretaniens des Maghrebides: La formation du jbel Tisirene (Rif, Maroc). *C. R. Acad. Sci.* **1999**, *328*, 701–709. [\[CrossRef\]](#)
62. Gübeli, A.A.; Hochuli, P.A.; Wildi, W. Lower Cretaceous turbiditic sediments from the Rif chain (Northern Morocco)—Palynology, stratigraphy and palaeogeographic setting. *Geol. Rundschau* **1984**, *73*, 1081–1114. [\[CrossRef\]](#)
63. Didon, J. Les séries à faciès mixte, numidien et grés-micacé, dans le Rif occidental (Maroc). *Bull. Soc. Geol. Fr.* **1978**, *6*, 304–307.
64. Lustrino, M.; Duggen, S.; Rosenberg, C.L. The Central-Western Mediterranean: Anomalous igneous activity in an anomalous collisional tectonic setting. *Earth-Sci. Rev.* **2011**, *104*, 1–40. [\[CrossRef\]](#)
65. Guerrero, F.; Martín-Algarra, A.; Martín-Martín, M. Tectono-sedimentary evolution of the “Numidian Formation” and Lateral Facies (southern branch of the western Tethys): Constraints for central-western Mediterranean geodynamics. *Terra Nov.* **2012**, *24*, 34–41. [\[CrossRef\]](#)
66. Chalouan, A.; El Mrihi, A.; El Kadiri, K.; Bahmad, A.; Salhi, F.; Hlila, R. Mauretanian flysch nappe in the northwestern Rif Cordillera (Morocco): Deformation chronology and evidence for a complex nappe emplacement. *Geol. Soc. Spec. Publ.* **2006**, *262*, 161–175. [\[CrossRef\]](#)
67. Michard, A.; Mokhtari, A.; Chalouan, A.; Saddiqi, O.; Rossi, P.; Rjmati, E.C. New ophiolite slivers in the External Rif belt, and tentative restoration of a dual Tethyan suture in the western Maghrebides. *Bull. Soc. Geol. Fr.* **2014**, *185*, 313–328. [\[CrossRef\]](#)

68. Andrieux, J. *La Structure du Rif Central: Étude des Relations entre la Tectonique de Compression et les Nappes de Glissement dans un Tronçon de la Chaîne Alpine*; Editions du Service géologique du Maroc: Rabat, Maroc, 1971; Volume 235.
69. Vidal, J.C. Present structure and evolution of the Rif chain (southern part of the arc of Gibraltar) since the Miocene. *Bull. Soc. Géol. Fr.* **1977**, *7*, 789–796. [[CrossRef](#)]
70. Crespo-Blanc, A.; de Lamotte, D.F. Structural evolution of the external zones derived from the Flysch trough and the South Iberian and Maghrebian paleomargins around the Gibraltar arc: A comparative study. *Bull. Soc. Geol. Fr.* **2006**, *177*, 267–282. [[CrossRef](#)]
71. Balsamo, F.; Aldega, L.; De Paola, N.; Faoro, I.; Storti, F. The signature and mechanics of earthquake ruptures along shallow creeping faults in poorly lithified sediments. *Geology* **2014**, *42*, 435–438. [[CrossRef](#)]
72. Bustin, R.M.; Barnes, M.A.; Barnes, W.C. Determining levels of organic diagenesis in sediments and fossil fuels. In *Diagenesis: Geosciences Canada Reprint, Fourth Series*; Geological Association of Canada: St. John's, NL, Canada, 1990; pp. 205–226.
73. Borrego, A.G.; Araujo, C.V.; Balke, A.; Cardott, B.; Cook, A.C.; David, P.; Flores, D.; Hámor-Vidó, M.; Hiltmann, W.; Kalkreuth, W. Influence of particle and surface quality on the vitrinite reflectance of dispersed organic matter: Comparative exercise using data from the qualifying system for reflectance analysis working group of ICCP. *Int. J. Coal Geol.* **2006**, *68*, 151–170. [[CrossRef](#)]
74. Beyssac, O.; Goffé, B.; Chopin, C.; Rouzaud, J.N. Raman spectra of carbonaceous material in metasediments: A new geothermometer—Beyssac—2002—Journal of Metamorphic Geology—Wiley Online Library. *J. Metamorph. Geol.* **2002**, *20*, 859–871. [[CrossRef](#)]
75. Beyssac, O.; Goffé, B.; Petitet, J.P.; Froigneux, E.; Moreau, M.; Rouzaud, J.N. On the characterization of disordered and heterogeneous carbonaceous materials by Raman spectroscopy. In *Spectrochimica Acta—Part A: Molecular and Biomolecular Spectroscopy, Proceedings of the Fifth International Conference on Raman Spectroscopy Applied to the Earth Sciences, Prague, Czech Republic, 12–15 June 2002*; Elsevier: Amsterdam, The Netherlands, 2003.
76. Lahfid, A.; Beyssac, O.; Deville, E.; Negro, F.; Chopin, C.; Goffé, B. Evolution of the Raman spectrum of carbonaceous material in low-grade metasediments of the Glarus Alps (Switzerland). *Terra Nov.* **2010**, *22*, 354–360. [[CrossRef](#)]
77. Guedes, A.; Valentim, B.; Prieto, A.C.; Rodrigues, S.; Noronha, F. Micro-Raman spectroscopy of collotelinite, fusinite and macrinite. *Int. J. Coal Geol.* **2010**, *83*, 415–422. [[CrossRef](#)]
78. Hinrichs, R.; Brown, M.T.; Vasconcellos, M.A.Z.; Abrashev, M.V.; Kalkreuth, W. Simple procedure for an estimation of the coal rank using micro-Raman spectroscopy. *Int. J. Coal Geol.* **2014**, *136*, 52–58. [[CrossRef](#)]
79. Wilkins, R.W.T.; Boudou, R.; Sherwood, N.; Xiao, X. Thermal maturity evaluation from inertinites by Raman spectroscopy: The “RaMM” technique. *Int. J. Coal Geol.* **2014**, *128–129*, 143–152. [[CrossRef](#)]
80. Zhou, Q.; Xiao, X.; Pan, L.; Tian, H. The relationship between micro-Raman spectral parameters and reflectance of solid bitumen. *Int. J. Coal Geol.* **2014**, *121*, 19–25. [[CrossRef](#)]
81. Ferralis, N.; Matys, E.D.; Knoll, A.H.; Hallmann, C.; Summons, R.E. Rapid, direct and non-destructive assessment of fossil organic matter via microRaman spectroscopy. *Carbon N. Y.* **2016**, *108*, 440–449. [[CrossRef](#)]
82. Lünsdorf, N.K. Raman spectroscopy of dispersed vitrinite—Methodical aspects and correlation with reflectance. *Int. J. Coal Geol.* **2016**, *153*, 75–86. [[CrossRef](#)]
83. Schmidt Mumm, A.; Inan, S. Microscale organic maturity determination of graptolites using Raman spectroscopy. *Int. J. Coal Geol.* **2016**, *162*, 96–107. [[CrossRef](#)]
84. Lupoi, J.S.; Fritz, L.P.; Parris, T.M.; Hackley, P.C.; Solotky, L.; Eble, C.F.; Schlaegle, S. Assessment of thermal maturity trends in Devonian–Mississippian source rocks using Raman spectroscopy: Limitations of peak-fitting method. *Front. Energy Res.* **2017**, *5*, 24. [[CrossRef](#)]
85. Schito, A.; Romano, C.; Corrado, S.; Grigo, D.; Poe, B. Diagenetic thermal evolution of organic matter by Raman spectroscopy. *Org. Geochem.* **2017**, *106*, 57–67. [[CrossRef](#)]
86. Henry, D.G.; Jarvis, I.; Gillmore, G.; Stephenson, M.; Emmings, J.F. Assessing low-maturity organic matter in shales using Raman spectroscopy: Effects of sample preparation and operating procedure. *Int. J. Coal Geol.* **2018**, *191*, 135–151. [[CrossRef](#)]
87. Henry, D.G.; Jarvis, I.; Gillmore, G.; Stephenson, M. A rapid method for determining organic matter maturity using Raman spectroscopy: Application to Carboniferous organic-rich mudstones and coals. *Int. J. Coal Geol.* **2019**, *203*, 87–98. [[CrossRef](#)]

88. Tuinstra, F.; Koenig, J.L. Raman Spectrum of Graphite. *J. Chem. Phys.* **1970**, *53*, 1126–1130. [[CrossRef](#)]
89. Friedel, R.A.; Carlson, G.L. Difficult carbonaceous materials and their infra-red and Raman spectra. Reassignments for coal spectra. *Fuel* **1972**, *51*, 194–198. [[CrossRef](#)]
90. Reich, S.; Thomsen, C. Raman spectroscopy of graphite. *Philos. Trans. R. Soc. A Math. Phys. Eng. Sci.* **2004**, *362*, 2271–2288. [[CrossRef](#)]
91. Pimenta, M.A.; Dresselhaus, G.; Dresselhaus, M.S.; Cançado, L.G.; Jorio, A.; Saito, R. Studying disorder in graphite-based systems by Raman spectroscopy. *Phys. Chem. Chem. Phys.* **2007**, *9*, 1276–1291. [[CrossRef](#)]
92. Pócsik, I.; Hundhausen, M.; Koós, M.; Ley, L. Origin of the D peak in the Raman spectrum of microcrystalline graphite. *J. Non. Cryst. Solids* **1998**, *227–230*, 1083–1086. [[CrossRef](#)]
93. Negri, F.; Castiglioni, C.; Tommasini, M.; Zerbi, G. A computational study of the Raman spectra of large polycyclic aromatic hydrocarbons: Toward molecularly defined subunits of graphite. *J. Phys. Chem. A* **2002**, *106*, 3306–3317. [[CrossRef](#)]
94. Negri, F.; di Donato, E.; Tommasini, M.; Castiglioni, C.; Zerbi, G.; Müllen, K. Resonance Raman contribution to the D band of carbon materials: Modeling defects with quantum chemistry. *J. Chem. Phys.* **2004**, *120*, 11889–11900. [[CrossRef](#)]
95. Di Donato, E.; Tommasini, M.; Fustella, G.; Brambilla, L.; Castiglioni, C.; Zerbi, G.; Simpson, C.D.; Müllen, K.; Negri, F. Wavelength-dependent Raman activity of D<sub>2h</sub> symmetry polycyclic aromatic hydrocarbons in the D-band and acoustic phonon regions. *Chem. Phys.* **2004**, *301*, 81–93. [[CrossRef](#)]
96. Li, C.Z. Some recent advances in the understanding of the pyrolysis and gasification behaviour of Victorian brown coal. *Fuel* **2007**, *86*, 1664–1683. [[CrossRef](#)]
97. Beny-Bassez, C.; Rouzaud, J.N. Characterization of carbonaceous materials by correlated electron and optical microscopy and Raman microspectroscopy. *Scan. Electron. Microsc.* **1985**, *1*, 119–132.
98. Ferrari, A.C.; Robertson, J. Interpretation of Raman spectra of disordered and amorphous carbon. *Am. Phys. Soc.* **2000**, *61*, 14095. [[CrossRef](#)]
99. Castiglioni, C.; Tommasini, M.; Zerbi, G. Raman spectroscopy of polyconjugated molecules and materials: Confinement effect in one and two dimensions. *Philos. Trans. R. Soc. A Math. Phys. Eng. Sci.* **2004**, *362*, 2425–2459. [[CrossRef](#)] [[PubMed](#)]
100. Schito, A.; Corrado, S. An automatic approach for characterization of the thermal maturity of dispersed organic matter Raman spectra at low diagenetic stages. *Geol. Soc. Lond. Spec. Publ.* **2018**, *484*. [[CrossRef](#)]
101. Sclater, J.G.; Christie, P.A.F. Continental stretching: An explanation of the post-mid-Cretaceous subsidence of the central North Sea basin. *J. Geophys. Res. Solid Earth* **1980**, *85*, 3711–3739. [[CrossRef](#)]
102. Endignoux, L.; Wolf, S.; Letouzey, J. Thermal and kinematic evolution of thrust basins: A 2D numerical model. *Pet. Tecton. Mob. Belts Paris Ed. Tech.* **1990**, *47*, 181–192.
103. Burnham, A.K.; Sweeney, J.J. A chemical kinetic model of vitrinite maturation and reflectance. *Geochim. Cosmochim. Acta* **1989**, *53*, 2649–2657. [[CrossRef](#)]
104. Sweeney, J.J.; Burnham, A.K. Evaluation of a simple model of vitrinite reflectance based on chemical kinetics. *Am. Assoc. Pet. Geol. Bull.* **1990**, *74*, 1559–1570.
105. Rimi, A. Mantle heat flow and geotherms for the main geologic domains in Morocco. *Earth Sci.* **1999**, *458–466*. [[CrossRef](#)]
106. Rimi, A.; Zeyen, H.; Zarhloule, Y.; Correia, A.; Carneiro, J.; Cherkaoui, T. *Structure Thermique de la Lithosphère à Travers la Limite des Plaques Ibérie—Afrique par Modélisation Intégrée du Flux de Chaleur, de la Densité et de la Topographie le Long d'un Transect N-S à 3 Ouest*; Bulletin de l'Institut Scientifique, section Sciences de la Terre: Rabat, Maroc, 2008; pp. 29–37.
107. Butler, R.W.H. Hydrocarbon maturation, migration and tectonic loading in the Western Alpine foreland thrust belt. *Geol. Soc. Lond. Spec. Publ.* **1991**, *59*, 227–244. [[CrossRef](#)]
108. Tissot, B.P.; Welte, D.H. *Petroleum Formation and Occurrence*, 2nd ed.; Science & Business Media: Berlin/Heidelberg, Germany, 1984; p. 699.
109. Corrado, S.; Chiara Invernizzi, C.; Marzzoli, S. Tectonic burial and exhumation in a foreland fold and thrust belt: The Monte Alpi case history (Southern Apennines, Italy). *Geodin. Acta* **2002**, *15*, 159–177. [[CrossRef](#)]
110. Liu, D.H.; Xiao, X.M.; Tian, H.; Min, Y.S.; Zhou, Q.; Cheng, P.; Shen, J.G. Sample maturation calculated using Raman spectroscopic parameters for solid organics: Methodology and geological applications. *Chinese Sci. Bull.* **2013**, *58*, 1285–1298. [[CrossRef](#)]

111. Jubb, A.M.; Botterell, P.J.; Birdwell, J.E.; Burruss, R.C.; Hackley, P.C.; Valentine, B.J.; Hatcherian, J.J.; Wilson, S.A. High microscale variability in Raman thermal maturity estimates from shale organic matter. *Int. J. Coal Geol.* **2018**, *199*, 1–9. [[CrossRef](#)]
112. Schito, A.; Corrado, S.; Aldega, L.; Grigo, D. Overcoming pitfalls of vitrinite reflectance measurements in the assessment of thermal maturity: The case history of the lower Congo basin. *Mar. Pet. Geol.* **2016**, *74*, 59–70. [[CrossRef](#)]
113. Guerrero, F.; Martín-Martín, M.; Tramontana, M. Evolutionary geological models of the central-western peri-Mediterranean chains: A review. *Int. Geol. Rev.* **2019**. [[CrossRef](#)]
114. Marshak, S. Salients, recesses, arcs, oroclines, and syntaxes—A review of ideas concerning the formation of map-view curves in fold-thrust belts. *AAPG Mem.* **2005**, *82*, 131–156.
115. Leblanc, D.; Olivier, P. Role of strike-slip faults in the Betic-Rifian orogeny. *Tectonophysics* **1984**. [[CrossRef](#)]
116. Leon, J.T. de Signification de la limite Jebha-Arbaoua (Maroc nord-occidental): Une rampe latérale au-dessus d'une discontinuité crustale héritée de la période de rifting. *J. Afr. Earth Sci.* **1997**. [[CrossRef](#)]
117. Benmakhlouf, M.; Galindo-Zaldívar, J.; Chalouan, A.; Sanz de Galdeano, C.; Ahmamou, M.; López-Garrido, A.C. Inversion of transfer faults: The Jebha-Chrafate fault (Rif, Morocco). *J. Afr. Earth Sci.* **2012**, *73–74*, 33–43. [[CrossRef](#)]
118. Vitale, S.; Zaghloul, M.N.; El Ouaragli, B.; Tramparulo, F.D.A.; Ciarcia, S. Polyphase deformation of the Dorsale Calcaire Complex and the Maghrebien Flysch Basin Units in the Jebha area (Central Rif, Morocco): New insights into the Miocene tectonic evolution of the Central Rif belt. *J. Geodyn.* **2015**, *90*, 14–31. [[CrossRef](#)]



© 2020 by the authors. Licensee MDPI, Basel, Switzerland. This article is an open access article distributed under the terms and conditions of the Creative Commons Attribution (CC BY) license (<http://creativecommons.org/licenses/by/4.0/>).